ACS APPLIED MATERIALS & INTERFACES

www.acsami.org

Research Article

Edge-Rich Bicrystalline 1T/2H-MoS_2 Cocatalyst-Decorated {110} Terminated CeO_2 Nanorods for Photocatalytic Hydrogen Evolution

Chengzhang Zhu, Qiming Xian, Qiuying He, Chuanxiang Chen,* Weixin Zou,* Cheng Sun, Shaobin Wang, and Xiaoguang Duan*

Cite This: *ACS Appl. Mater. Interfaces* 2021, 13, 35818–35827

Read Online

ACCESS | Metrics & More | Article Recommendations | Supporting Information

ABSTRACT: Developing all-solid-state Z-scheme systems with highly active photocatalysts are of huge interest in realizing long-term solar-to-fuel conversion. Here we reported an innovative hybrid of {110}-oriented CeO_2 nanorods with edge-enriched bicrystalline 1T/2H-MoS_2 coupling as efficient photocatalysts for water splitting. In the composites, the metallic 1T phase acts as an excellent solid state electron mediator in the Z-scheme, while the 2H phase and CeO_2 are the adsorption sites of the photosensitizer and reactant (H_2O), respectively. Through optimal structure and phase engineering, 1T/2H-MoS_2@CeO_2 heterojunctions simultaneously achieve high charge separation efficiency, proliferated density of exposed active sites, and excellent affinity to reactant molecules, reaching a superior hydrogen evolution rate of 73.1 μmol/h with an apparent quantum yield of 8.2% at 420 nm. Furthermore, density functional theory calculations show that 1T/2H-MoS_2@CeO_2 possesses the advantages of intensive electronic interaction from the built-in electric field (negative MoS_2 and positive charged CeO_2) and reduced H_2O adsorption/dissociation energies. This work sheds light on the design of on-demand noble-metal-free Z-scheme heterostructures for solar energy conversion.

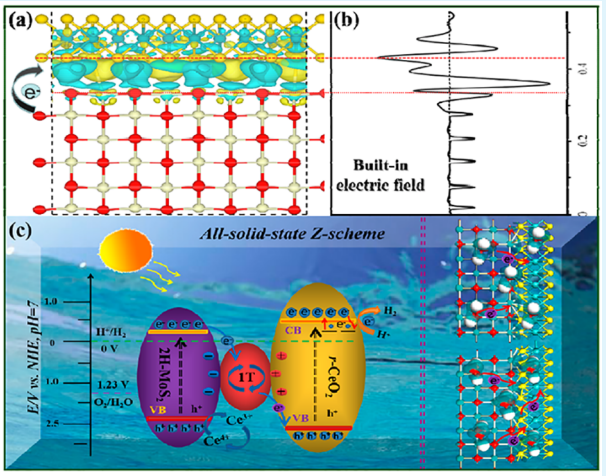

KEYWORDS: *bicrystalline 1T/2H-MoS_2, water splitting, electronic interaction, Z-scheme heterojunction, H_2O reactant adsorption*

INTRODUCTION

Hydrogen is a clean fuel with high-energy density that holds great promise for solving the global energy crisis and reducing carbon emissions.[1−4] Among the available technologies, sunlight-driven water splitting by semiconductors is an attractive and green approach to convert solar energy into renewable hydrogen energy.[5,6] With rich oxygen defects, specific $4f^15d^1$ orbitals, and superior oxygen storage-release ability in Ce^{4+}/Ce^{3+} reversibility pairs, the popular rare earth ceria oxides (CeO_2) exhibit extensive applications in various fields, especially for photocatalysis and solar-to-fuel conversion.[7−10] Nevertheless, the results are still far from meeting the practical demand of efficiency because of the narrow spectral photoresponse and rapid electron−hole recombination on CeO_2 before migrating to the surface for reactions.[11,12] Although the noble metals have been proven to be efficient cocatalysts for photocatalysis, the upscale application is restricted by their high cost and scarcity.[13−17] It is imperative to explore highly active and inexpensive noble-metal-free cocatalysts with suitable band structures complementary to that of CeO_2, creating an artificial junction to enhance light absorption and interfacial charge separation efficiency.

Two-dimensional (2D) layered transition metal dichalcogenides with impressive structural, optical, and electronic properties have attracted tremendous attention in photocatalysis.[18−21] In particular, three stacked atomic layers (S−Mo−S) of molybdenum disulfide (MoS_2), with unsaturated S atoms on exposed edges as reactive sites, are favorable for photocatalytic hydrogen evolution (PHE), enabling MoS_2 to be an ideal alternative to noble-metal cocatalysts.[22−25] Despite the above fascinating merits, the number of generated active sites is excessively restricted to its edge population. To this end, aside from reducing the thickness of MoS_2 nanosheets (NSs), recent studies have applied phase engineering to maximize the density of edging sites.[26,27] Actually, MoS_2 primarily exists in two common crystal phases; the stable 2H trigonal prismatic phase is thermodynamically favored, whereas the hydrophilic 1T octahedral metallic phase has higher

Received: May 25, 2021
Accepted: July 12, 2021
Published: July 26, 2021

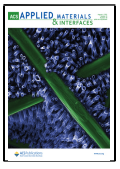

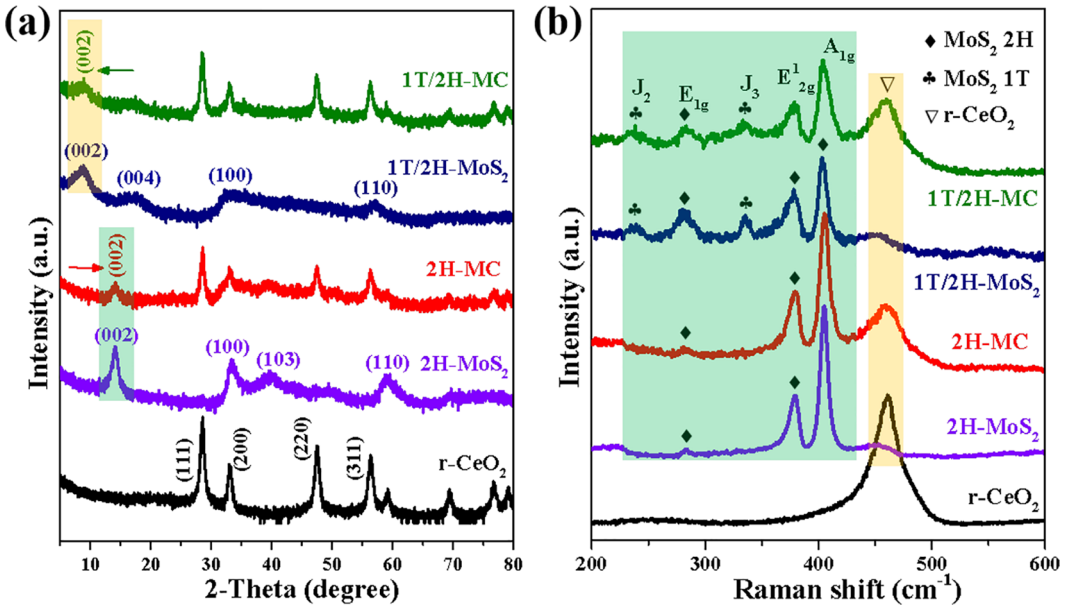

Figure 1. (a) XRD patterns and (b) Raman spectra of r-CeO_2, 2H-MoS_2, 1T/2H-MoS_2, 2H-MC, and 1T/2H-MC.

electrical conductivity which can promote charge transfer kinetics and realize low-loss electrical transport.[28−31] By regulating the phase transformation, more active sites will be preferentially exposed on both the basal plane and edges, inducing an edge-rich bicrystalline (1T and 2H phases) nanostructure for efficient photocatalytic water splitting. The 2H phase serves as a photosensitizer for visible light harvesting, and the 1T phase acts as an electron conductor/acceptor. Moreover, from a practical point of view, an integrated system of two individual components tightly connected by a charge-transport unit is desirable.[32,33] Especially, the Z-scheme photocatalytic system, inspired by natural photosynthesis, retains a higher redox capacity that is beneficial to producing holes and radicals. Meanwhile, a Z-scheme charge-transfer pathway is more physically feasible compared to the traditional type-II heterojunctions. All-solid-state Z-scheme heterojunctions based on 1T/2H-MoS_2 will not only facilitate interfacial electrons transfer, but also strengthen the stability to prevent the transformation of unstable 1T phase into 2H phase. Therefore, noble-metal-free 1T/2H-MoS_2@CeO_2 composites is promising for PHE in light of efficient visible-light absorption, fast charge separation and transport, providing rich Ce^{3+}/Ce^{4+} redox sites and strong interfacial electronic interactions.

Herein, we design an all-solid-state Z-scheme heterostructure of edge-rich bicrystalline ultrathin 1T/2H-MoS_2 NSs coupled with one-dimensional (1D) CeO_2 nanorods and investigate the synergistic effect of each component on PHE activities under visible light irradiation. The innovative heterostructure enables broader solar absorption, shorter electron-diffusion distance, abundant Ce^{3+}/oxygen vacancies, and Ce^{3+}/Ce^{4+} redox sites. The robust 2D-1D geometry also allows intimate interfaces interactions. These factors collectively lead to improved PHE activity of the ternary composites compared with bare CeO_2, 2H-MoS_2, and 1T/2H-MoS_2. Furthermore, the electron density distribution and adsorption/dissociation ability of reactant H_2O molecules on the 1T/2H-MoS_2@CeO_2 heterojunction were investigated by density functional theory (DFT). A schematic illustration of the plausible reaction mechanism was also proposed.

EXPERIMENTAL SECTION

Synthesis of {110}-Oriented CeO_2 Nanorods. {110} facet exposed CeO_2 nanorods (r-CeO_2) were fabricated as follows: $CeCl_3 \cdot 7H_2O$ (2 mmol) was ultrasonically dissolved in ultrapure water, then NaOH aqueous solution (6 M) was injected dropwise under vigorous stirring for 0.5 h. Subsequently, the above mixture was sealed into a 50 mL Teflon-lined stainless-steel autoclave and heated at 140 °C for 18 h. After repeated washing until Cl^- removal (pH = 7) and oven drying, the obtained products were calcined in a muffle furnace at 450 °C for 3 h.

Coupling r-CeO_2{110} with Edge-Rich Ultrathin 1T/2H-MoS_2 NSs. For the synthesis of r-CeO_2{110}@1T/2H-MoS_2, 0.04 g of newly prepared r-CeO_2 and $(NH_4)Mo_7O_{24} \cdot 4H_2O$ (0.3 mmol) were dispersed in ultrapure water in a ultrasonic bath for 1 h. Afterward, appropriate amounts of KSCN and $CO(NH_2)_2$ were gradually added into the above faint yellow suspension while stirring vigorously. The resultant homogeneous suspension was kept at 180 °C for 20 h for hydrothermal treatment. Upon cooling naturally to room temperature, the black precipitate was washed with ultrapure water and ethanol for several times before drying at 60 °C, which was abbreviated as 1T/2H-MC. For comparison, the collected composites were annealed at 500 °C under Ar atmosphere and defined as 2H-MC. The synthesis processes of 2H-MoS_2 and 1T/2H-MoS_2 were similar to the above procedure in the absence of r-CeO_2.

RESULTS AND DISCUSSION

Crystal Structures, Morphologies, and Texture Properties. The crystallographic structures of r-CeO_2, 2H-MoS_2, 1T/2H-MoS_2, 2H-MC, and 1T/2H-MC were investigated using XRD analysis (Figure 1a). Typically, a series of diffraction peaks located at 28.5°, 33.1°, 47.5°, and 56.3° were well indexed as (111), (200), (220), and (311) crystal planes of cubic phase CeO_2, respectively (space group $Fm\bar{3}m$, JCPDS card no. 34-0394).[34,35] Owing to the introduction of 1T phase, a new (004) peak appeared, simultaneously the (002) peak of 1T/2H-MoS_2 shifted toward lower angles in comparison with the dominant peaks of 2H-MoS_2, suggesting that the 2H/1T mixed phases were formed. Moreover, such a blue shift indicated the increased interlayer distance in 1T/2H-MoS_2 due to the insertion of ammonium ions, which is beneficial for electron transport.[36,37] Similar phenomena have

https://doi.org/10.1021/acsami.1c09651
ACS Appl. Mater. Interfaces 2021, 13, 35818−35827

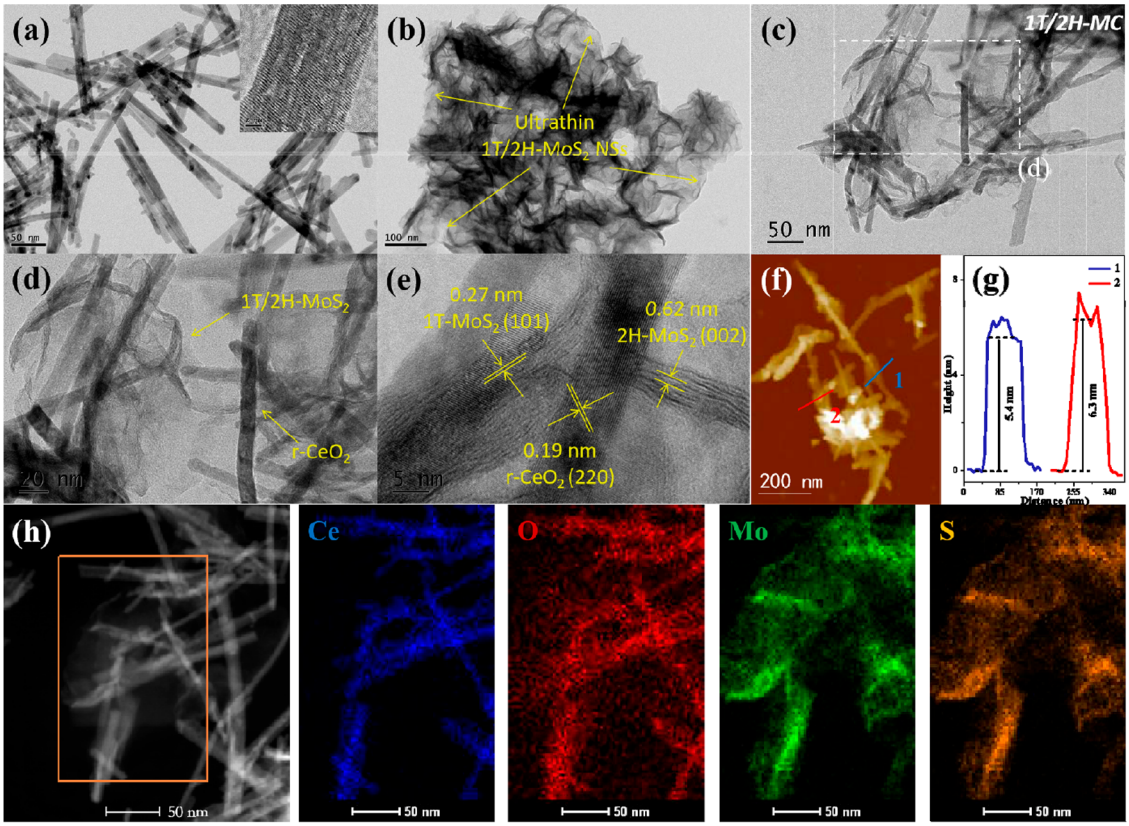

Figure 2. TEM images of (a) r-CeO_2, (b) 1T/2H-MoS_2, and (c, d) 1T/2H-MC at different magnifications. (e) HRTEM image, (f) AFM image and corresponding (g) height profile, and (h) HAADF-STEM image and corresponding elemental mappings (Ce, O, Mo, and S) of 1T/2H-MC heterojunction.

been found in 2H-MC and 1T/2H-MC, further confirming the existence of metallic 1T-MoS_2 with high stability. Upon decoration of 1T/2H-MoS_2 with r-CeO_2, those typical peaks were still detected in the composites, revealing the successful coupling of the two moieties with good homogeneity and crystallinity.

Raman spectroscopy was performed to determine the phase of transition metal disulfides. As shown in Figure 1b, three representative vibration peaks at around 283, 379, and 404 cm^{-1} were observed in 2H-MoS_2, 2H-MC, 1T/2H-MoS_2, and 1T/2H-MC, which are ascribed to E_{1g}, in-plane Mo−S phonon mode (E^1_{2g}), and out-of-plane Mo−S mode (A_{1g}) of the 2H phase, respectively.[2] Notably, the emerged new bands at approximately 238 and 336 cm^{-1} in pristine 1T/2H-MoS_2 and 1T/2H-MC were ascribed to the J_2 and J_3 vibration modes of S−Mo−S bonds accordingly, which only occurred in 1T-phase of MoS_2.[38] This verified the introduction of a considerable amount of 1T phase ingredient embedded in 2H-MoS_2, which are in accordance with the above XRD analysis. Additionally, the Raman shifts of 1T/2H-MC exhibited typical bands corresponding to r-CeO_2 (460 cm^{-1}) and 1T/2H-MoS_2, further demonstrating that the metallic 1T phase-based hybrid is obtained.

TEM and AFM were performed to obtain the micro-topography and internal structure information on the as-prepared samples. Figure 2a displays that pristine CeO_2 possesses uniform nanorod-like shapes with the length of 200−400 nm and an average diameter of about 20 nm (Figure S1 of the Supporting Information, SI). The layered 1T/2H-MoS_2 hybrid composes abundant edge-exposing ultrathin NSs (Figure 2b). After coupling 1*T*/2H-MoS_2 with r-CeO_2, the above-mentioned two catalysts are in close contact with each other as evidenced by TEM at different magnifications (Figure 2c,d) and AFM image (Figure 2f). Simultaneously, according to the AFM image of 1T/2H-MC and its corresponding height profiles (Figure 2g), the thickness of 1T/2H-MoS_2 was measured to be 5.4 to 6.3 nm. The ultrathin 2D structure may lead to rapid in-plane charge transfer and facilitate the migration of efficient photoexcited electrons to the surface.[39] As shown in the high-resolution TEM (HRTEM) image (Figure 2e), the crystal lattice was 0.19 nm, which corresponded to the (220) plane, manifesting that the primary plane of r-CeO_2 was {110} facet.[40,41] The widely separated fringes with the interplanar spacing of 0.62 and 0.27 nm were severally assigned as the (002) plane of 2H-MoS_2 and the (101) plane of 1T-MoS_2.[42] Moreover, TEM elemental mapping (Figure 2h) reveals the homogeneous distribution of Ce, O, Mo, and S in the whole 1T/2H-MC heterostructure, further conforming the intimately interacted interfaces, rather than physically mixing. Therefore, the 2D ultrathin structure of 1T/2H-MoS_2 NSs are successfully decorated with 1D CeO_2 nanorods with {110} facets.

The textural property of pure r-CeO_2, 2H-MoS_2, 1T/2H-MoS_2, 2H-MC, and 1T/2H-MC were investigated by nitrogen adsorption−desorption test, and the results are depicted in Figure S2. Obviously, all the catalysts display similar type-IV isotherms with hysteresis loops, elucidating the existence of mesoporous structure.[43,44] For clear comparison, the detailed specific surface area (SSA), pore volume, and pore size distribution of as-prepared photocatalysts are summarized in

https://doi.org/10.1021/acsami.1c09651
ACS Appl. Mater. Interfaces 2021, 13, 35818−35827

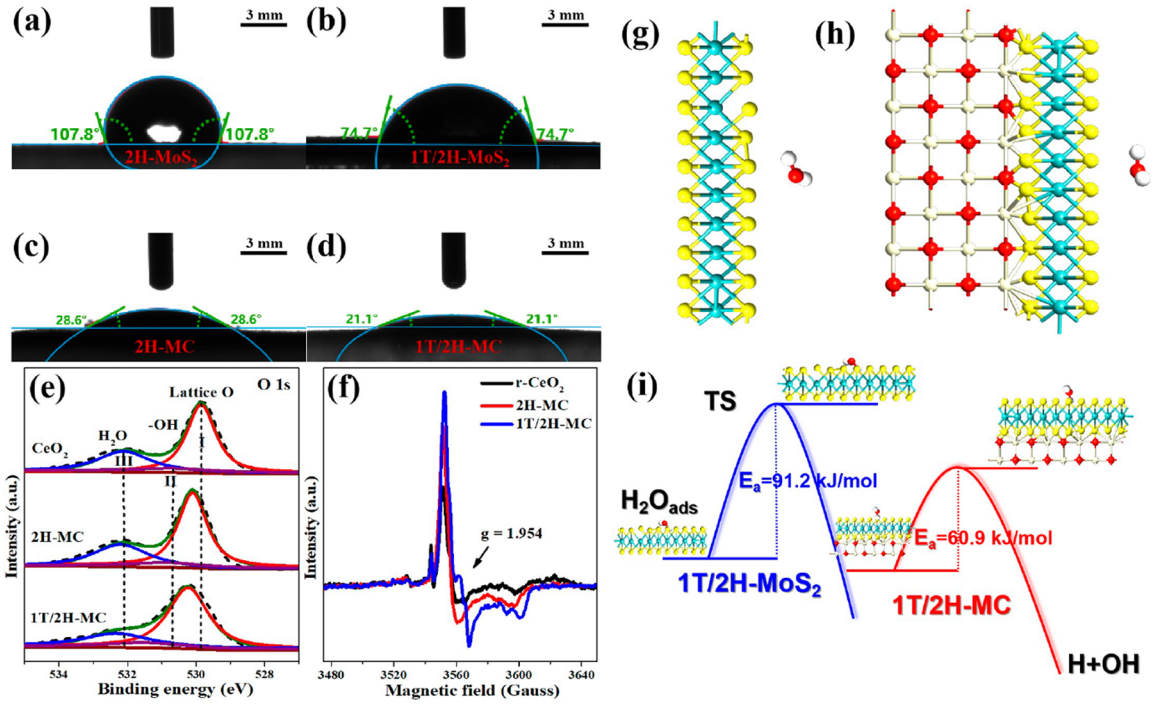

Figure 3. Contact angle measurements of (a) 2H-MoS_2, (b) 1T/2H-MoS_2, (c) 2H-MC, and (d) 1T/2H-MC. (e) XPS-O 1s and (f) EPR spectra of r-CeO_2, 2H-MC, and 1T/2H-MC. Optimized geometries of (g) 1T/2H-MoS_2, (h) 1T/2H-MC, and (i) with the corresponding activation energies of H_2O dissociation to OH and H for related states.

Table S1. It is worth noting that 1T/2H-MoS_2 NSs have a higher BET SSA of 53 m^2g^{-1} than 2H-MoS_2(30 m^2g^{-1}), which is favorable for exposing more active edge sites.[23,45] Abnormally, SSAs of both 2H-MC and 1T/2H-MC decrease slightly compared to bare r-CeO_2. Considering the BET results, it can be concluded that SSA in this work may not be the crucial factor for the improved photocatalytic performance.

Optical and Photoelectrical Properties. Since the light absorption capacity is of great significance to photocatalysis, the optical properties of the samples were probed by UV−vis DRS in Figure S3a. Notably, photosensitive 2H-MoS_2 with large absorption coefficient leads to a significant change of 1T/2H-MC hybrids in the shape of the absorption edge, enabling the harvest of more visible light. Generally, the corresponding band gap energies (E_g) depicted in Figure S3b are determined according to the Kubelka−Munk function.[46,47] Consequently, the E_g values are estimated to be 1.91 eV for 2H-MoS_2, and 2.96 eV for r-CeO_2. Moreover, combining with the XPS valence spectra (Figure S4c,d) and the equation of $E_{CB} = E_{VB} - E_g$, the conduction band (CB) values of r-CeO_2 and 2H-MoS_2 locate at −0.42 and −0.2 eV, respectively. On the basis of the well-matched bandgap structures and the metallic properties of the 1T phase, all-solid-state Z-scheme 1T/2H-MC heterojunctions are constructed.

Figure S5 presents the time-resolved PL spectra of different catalysts under 325 nm laser excitation. Evidently, a fast decay feature in the nanosecond scale was found in several catalysts after fitting the decay curves via the biexponential function.[48] The average lifetime (τ_{PL}) can be determined by the equation: $\tau_{PL} = (A_1\tau_1^2 + A_2\tau_2^2)/(A_1\tau_1 + A_2\tau_2)$, where τ_1 and τ_2 are separately referred to the short lifetime and long lifetime, reflecting the radiative recombination and nonradiative relaxation processes of photoinduced charge carriers, respectively.[49,50] The fitted parameters are listed in the inset of Figure S5a−e and Table S2. Clearly, the calculated τ_{PL} of 1T/2H-MC (6.39 ns) was dramatically prolonged with respect to 2H-MC (5.35 ns), r-CeO_2 (3.24 ns), 2H-MoS_2 (1.29 ns), and 1T/2H-MoS_2 (1.55 ns). The results suggested that 1T/2H-MC heterojunctions significantly accelerated charge transfer, owing to the synergy of the metallic 1T phase of MoS_2 and the interacted $Ce^{3+/4+}$ redox couples.

To further understand the advantage of 1T/2H-MC on the separation behavior of the photogenerated charge carries, we measured the photocurrent responses of r-CeO_2, 2H-MoS_2, 2H-MC, 1T/2H-MoS_2, and 1T/2H-MC with several on−off cycles of intermittent visible-light irradiation (Figure S6a). Owing to the metallic nature of 1T-MoS_2, the prepared electrode with 1T/2H-MC exhibits a noticeable improvement compared to 2H-MC. Not surprisingly, the photocurrent density of 1T/2H-MC markedly risen to 0.043 μA, which is roughly 10, 5.4, and 3.1 times greater than 2H-MoS_2, 1T/2H-MoS_2, and r-CeO_2, respectively. In particular, the EIS profiles of as-prepared catalysts showed similar variation trends (Figure S6b). Therein, 1T/2H-MC heterojunction presented the shortest arc radius, reflecting the minimum electrical resistance.[51] As a result, it can be reasonably concluded that the presence of metallic 1T-phase of MoS_2 is beneficial for the high-efficiency separation and transfer of photogenerated charges within the 1T/2H-MC heterostructures, thus effectively inhibiting the electron−hole recombination.

Reactant H_2O Adsorption/Dissociation. The adsorption and dissociation of reactant H_2O molecules on the surface of photocatalysts are vital steps in PHE reactions.[52] The contact-angle and XPS-O 1s measurements were conducted to compare the hydrophilic properties of 2H-MoS_2, 2H-MC, 1T/2H-MoS_2, and 1T/2H-MC. In Figure 3a−d, after coupling with r-CeO_2, the values of the contact angles over 2H-MC and 1T/2H-MC dramatically descend to 28.6°, and 21.1°,

https://doi.org/10.1021/acsami.1c09651
ACS Appl. Mater. Interfaces 2021, 13, 35818−35827

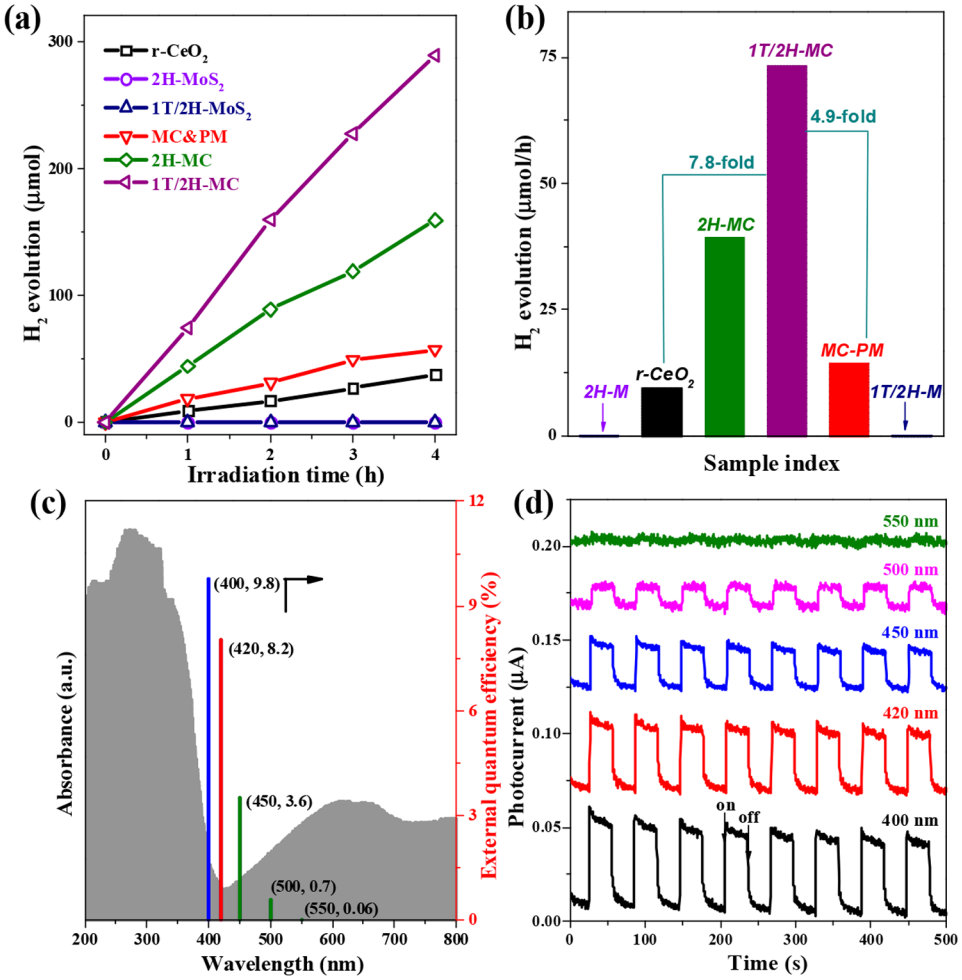

Figure 4. (a) Time courses of PHE activity and (b) average PHE rate of r-CeO_2, 2H-MoS_2, 1T/2H-MoS_2, MC-PM, 2H-MC, and 1T/2H-MC under visible-light irradiation. (c) AQY of 1T/2H-MC and (d) wavelength-dependent transient photocurrent responses of 1T/2H-MC with several on/off illumination cycles.

respectively, in comparison with those of 1T/2H-MoS_2 (74.7°) and 2H-MoS_2 (107.8°). Therefore, the affinity of H_2O molecules to 1T/2H-MC is greatly enhanced, and the accessible surface is favorable to decrease the energy barriers in PHE.

In addition, the XPS spectrum of O 1s (Figure 3e) was analyzed, and the broad peak can be fitted into two peaks. The peak centered at ca. 529.8 eV originates from the lattice oxygen of CeO_2, and the peak at ca. 530.6 and 532.1 eV are associated with the hydroxyl group (−OH) and chemisorbed water, respectively.[53] Compared with r-CeO_2, the binding energies of the lattice oxygen of CeO_2 on 1T/2H-MC shifts to higher values, indicating that more oxygen vacancies were created in 1T/2H-MC. Generally, Ce^{3+} species and oxygen vacancies are simultaneously formed, which play a crucial role in enhancing the interfacial interaction and H_2O adsorption.[41] On the basis of that, the superior hydrophilic property of 1T/2H-MC can be attributed to the high level of Ce^{3+} species.

ESR spectra further confirmed that 1T/2H-MC has a higher population of low-valence Ce^{3+}. The typical signal of g = 1.954 belongs to Ce^{3+} species,[54] and the signal intensity of 1T/2H-MC is more intensive than that of 2H-MC (Figure 3f), implying that more Ce^{3+} species formed on 1T/2H-MC. Consequently, in terms of the measurements of the contact-angle, O 1s spectra, and ESR, a greater amount of H_2O molecules will adsorb on 1T/2H-MC because of the rich Ce^{3+} sites, which is beneficial for the following H_2O activation and hydrogen evolution.

Furthermore, the activation energies of H_2O molecule dissociation on 1T/2H-MoS_2 and 1T/2H-MC samples were investigated by DFT calculations for comparison. As depicted in Figure 3g,h, the activation energies over 1T/2H-MoS_2 and 1T/2H-MC were calculated to be 91.2 and 60.9 kJ/mol, respectively, ordered by 1T/2H-MoS_2 > 1T/2H-MC as illustrated in Figure 3i. The different activation energies of H_2O molecule dissociation suggest that the reactant molecule (H_2O) is preferably dissociated into H and OH species on the Z-scheme 1T/2H-MC photocatalyst, not on 1T/2H-MoS_2. Similar results are found for 2H-MoS_2 and 2H-MC (Figure S7). Therefore, the results of the hydrophilic property and H_2O dissociation demonstrate that, compared with other photocatalysts, the 1T/2H-MC heterojunction with more Ce^{3+} species attained the lowest adsorption and dissociation energies of the water molecule toward efficient water splitting.

Photoactivity of Hydrogen Generation. The performances of photocatalytic water splitting over different samples were evaluated in the existence of the sacrificial reagents (0.5 M Na_2S/Na_2SO_3 solution) under irradiation of the visible spectrum for 4 h. As illustrated in Figure 4a,b, a relatively low H_2 evolution rate was detected for r-CeO_2 owing to its low

https://doi.org/10.1021/acsami.1c09651
ACS Appl. Mater. Interfaces 2021, 13, 35818−35827

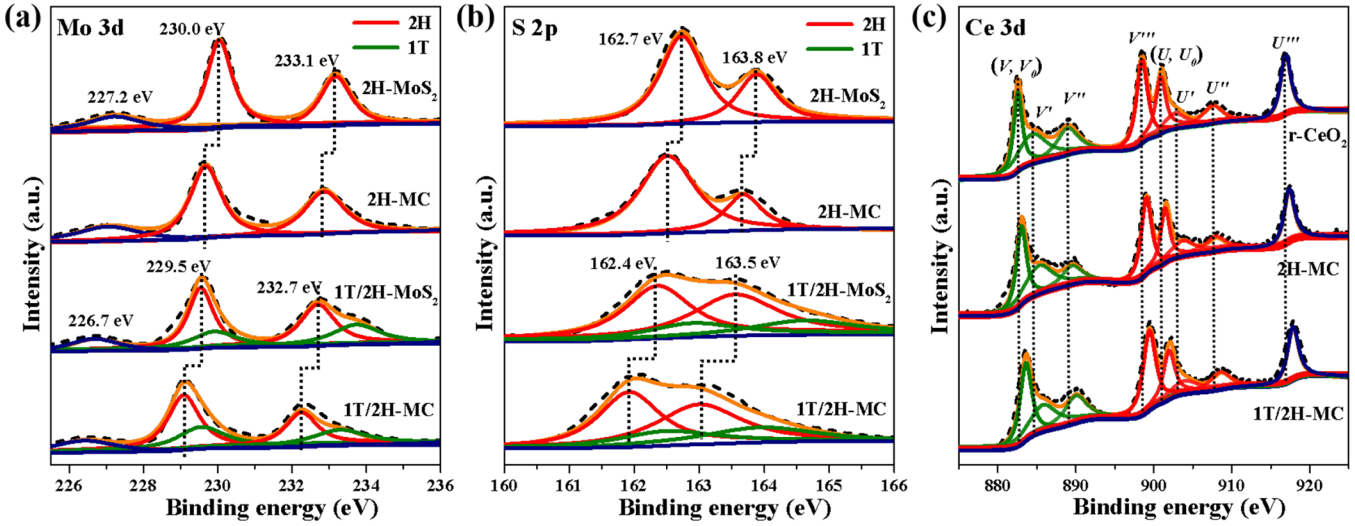

Figure 5. High-resolution XPS spectra of (a) Mo 3d, (b) S 2p, and (c) Ce 3d region for 2H-MoS_2, 1T/2H-MoS_2, r-CeO_2, 2H-MC, and 1T/2H-MC heterojunction.

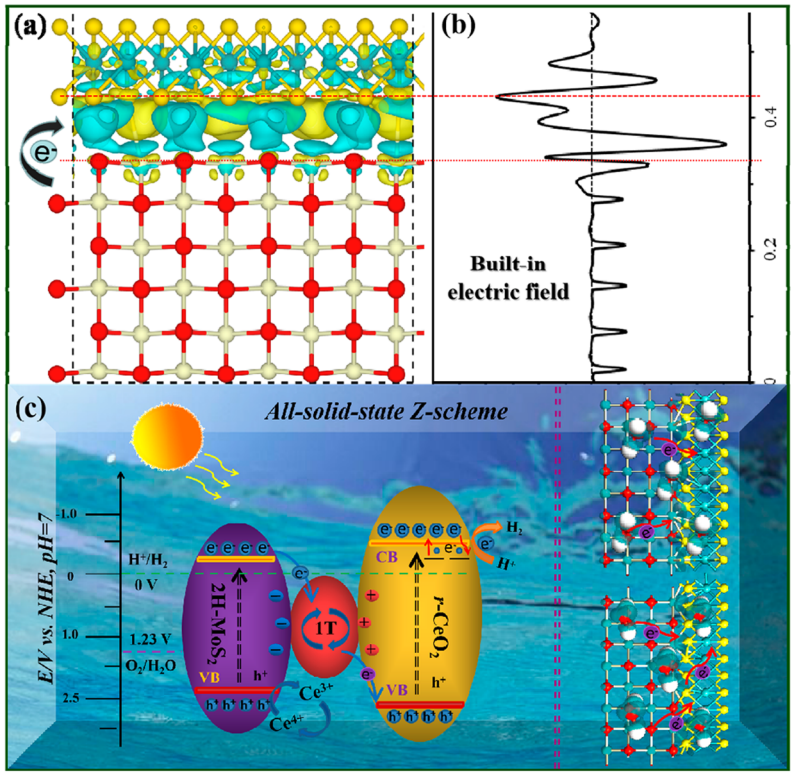

Figure 6. (a) 3D interfacial charge densities for 1T/2H-MC. Cyan and yellow regions represent electron depletion and accumulation, respectively. (b) Planar averaged charge density difference as a function of fractional position in the *Z*-direction. (c) Proposed photocatalytic mechanism for the enhanced PHE in all-solid-state Z-scheme 1T/2H-MC heterojunctions.

light utilization and fast electron−hole recombination. No observable H_2 was generated for bare 2H-MoS_2 and 1T/2H-MoS_2, while the binary hybrids of 1T/H-MC and 2H-MC display drastically enhanced PHE activities. Particularly, owing to the photosensitive 2H-MoS_2, abundant activated sites of CeO_2, and the electron mediator of metallic 1T phase, the all-solid-state Z-scheme 1T/H-MC shows the highest PHE efficiency (288.7 μmol) and production rate (73.1 μmol/h), which are approximately 7.8- and 4.9-fold greater than that of pure r-CeO_2 and a physical mixture of two moieties (defined as MC-PM), respectively. This value is also superior to the majority of previously reported MoS_2-based photocatalysts (Table S3). Furthermore, the wavelength dependence of apparent quantum yield (AQY) was tested to study the solar energy conversion efficiency. Figure 4c shows that the AQY of 1T/2H-MC was evaluated to be 8.2% at 420 nm, which distinctly decreased at longer wavelengths. Likewise, the photocurrent responses of 1T/2H-MC (Figure 4d) at different wavelengths are consistent with the variation tendency of the above-mentioned AQY. To minimize the effect of SSA on PHE

https://doi.org/10.1021/acsami.1c09651
ACS Appl. Mater. Interfaces 2021, 13, 35818−35827

rate, the photoactivity of different samples were normalized. The normalized rate constants (k') are listed in Table S4. The results indicated that SSAs of the as-prepared photocatalysts impact significantly on their PHE performances. During the consecutive six runs over 24 h (Figure S8), no noticeable decline in PHE performance was detected. XRD results in Figure S9 showed that no obvious change of the crystal phase was found in the reused 1T/2H-MC, validating its impressive photostabilization for multiple cycles.

Interfacial Interactions and Proposed Reaction Mechanism. As it is well-known, the optical, photoelectrical, and catalytic performances are intimately related to the interfacial electronic interaction of heterojunction photocatalysts.[55,56] XPS was carried out to investigate the interfacial effects and surface electronic structure of the samples. The XPS characterization well indicates the emergence of 1T-phase MoS_2. The typical peaks at 230.0 and 233.1 eV belong to the binding energies of Mo^{4+} $3d_{5/2}$ and $Mo^{4+}3d_{3/2}$ electrons in 2H-MoS_2, both of which shift to the lower energies (Figure 5a).[57] Similarly, for the S 2p spectrum, additional two peaks are observed besides the featured doublet peaks of 2H-MoS_2 (Figure 5b), and the change of these peaks are still derived from the 1T phase.[58] Figure 5c shows that the Ce 3d core level spectrum can be divided into the spin splitting orbits of $3d_{5/2}$ and $3d_{3/2}$, V' and U' corresponding to Ce^{3+}, while those of Ce^{4+} are regarded as V, V'', V''', U, U'', and U'''. Notably, rich Ce^{3+} species in 1T/2H-MC were reported favorable for water adsorption and the subsequent surface redox reaction (hydrogen evolution).[41,59]

In contrary to Mo 3d and S 2p spectra of 2H-MC and 1T/2H-MoS_2, it is observed that the binding energy of 1T/2H-MC shifts to lower values, suggesting that more electrons are accumulated on MoS_2 in the 1T/2H-MC hybrids. For the Ce 3d XPS spectra of r-CeO_2,1T/2H-MC and 2H-MC, the peak positions of 1T/2H-MC shift to higher energies, suggesting that more electrons are transferred from Ce to attain a higher valence state. Therefore, an intensive built-in electric field is presented upon the formation of the 1T/2H-MC composites, leading to the positive-charged r-CeO_2 and negative-charged MoS_2.

To confirm the formed built-in electric field of 1T/2H-MC in depth, the interfacial electron densities of r-CeO_2 and 1T/2H-MoS_2 were theoretically calculated. The charge densities of 1T/2H-MoS_2@r-CeO_2{110} are shown in Figure 6a, in which the cyan and yellow regions separately referred to the electron depletion and accumulation. Clearly, a richer region of charge accumulation was observed on MoS_2, whereas the charge depletion occurred on the Ce and O atoms of r-CeO_2. Moreover, the discrepancy of interactions can be expressed as $\Delta\rho = \rho(1T/2H\text{-}MC) - \rho(r\text{-}CeO_2) - \rho(MoS_2)$, where $\rho(1T/2H\text{-}MC)$, $\rho(r\text{-}CeO_2)$, and $\rho(MoS_2)$ are the electron densities of the hybrid, r-CeO_2, and MoS_2 surfaces in the same configuration, respectively (Figure 6b). Similar to the XPS results, both the electron accumulation on MoS_2 and depletion of r-CeO_2 visually manifested that positively charged r-CeO_2 and negative-charged MoS_2 on Z-scheme 1T/2H-MC are beneficial for charge separation.

On the basis of these experimental and theoretical data, a probable photoinduced carrier transport mechanism of Z-scheme 1T/2H-MC heterojunction is proposed in Figure 6c. The superior visible-light PHE activity can be attributed to the following factors:

(i) For the innovative all-solid-state Z-scheme 1T/2H-MC photocatalyst, 1T-phase of MoS_2 with metal-like conductivity acts as an electron acceptor/mediator, which kinetically accelerates the charge transfer at the interfaces. Meanwhile, 2H-MoS_2 dramatically enhances the light-harvesting capacity and promotes the formation of more carriers for PHE reaction thermodynamically. More importantly, the edge-rich ultrathin NSs structures endow 1T/2H-MC with populated exposed active sites and a shortened pathway for charge transfer.

(ii) Ce^{3+} species of 1T/2H-MC is beneficial for reactant H_2O adsorption and dissociation, leading to the decreased energy barriers for superior PHE efficiency. In addition, the accumulated holes on 2H-MoS_2 will result in partial oxidation via converting Ce^{3+} to Ce^{4+}, which are conducive to prolonging the lifetime of free carriers over 1T/2H-MC. As the redox centers, the presence of Ce^{4+} allows electron trapping to inhibit charge recombination, while Ce^{3+} defects/oxygen vacancies render H_2O molecules more accessible to the adsorption/active sites.

(iii) Driven by the established intensive built-in electric field, i.e., positively charged r-CeO_2 and negatively charged MoS_2 in 1T/2H-MC, the photoinduced electrons tend to migrate from the CB of 2H-MoS_2 to r-CeO_2 via the metallic 1T-MoS_2 shuttle in an all-solid-state Z-scheme heterojunction. The resulting photoexcited electrons on the CB of r-CeO_2 possess more negative potential with a stronger driving force to reduce H_2O molecules. Simultaneously, the backflow of electrons is suppressed, thus high-efficiency electron−hole separation can be achieved. Furthermore, the well-constructed heterostructure can protect 1T-MoS_2 in the Na_2S/Na_2SO_3 solution from photocorrosion and phase transition, giving rise to the outstanding PHE activity and cyclic stability.

CONCLUSIONS

In summary, a facile protocol was developed to synthesize r-CeO_2{110}-based hybrid photocatalysts containing a cocatalyst of edge-rich ultrathin 1T/2H-MoS_2 NSs. Phase engineering renders the photosensitizer 2H phase to become excited and produce abundant photoelectrons and holes, while the conductive 1T phase facilitates the charge-transfer kinetics and serves as an electron mediator in the all-solid-state Z-scheme system. Moreover, Ce^{3+} species of r-CeO_2{110} is provided with better affinity to the reactant (H_2O molecules) and decreased energy barrier. Therefore, the optimized 1T/2H-MoS_2@CeO_2 exhibits an excellent PHE performance with an AQY of 8.2% (420 nm). This study indicates that the development of noble-metal-free cocatalyst-based all-solid-state Z-scheme heterostructures are feasible and have great potential for PHE under visible-light irradiation.

ASSOCIATED CONTENT

Supporting Information

The Supporting Information is available free of charge at https://pubs.acs.org/doi/10.1021/acsami.1c09651.

Experiment details (materials, characterization, photocatalytic test, and theoretical calculation); average diameter distribution of bare r-CeO_2; N_2 adsorption−desorption isotherms, UV−vis DRS, high-resolution

https://doi.org/10.1021/acsami.1c09651
ACS Appl. Mater. Interfaces 2021, 13, 35818−35827

XPS-VB, time-resolved PL, EIS, and transient photocurrent response of samples; XRD spectra of 1T/2H-MC heterojunction after photocatalysis; schematic illustration of activation energies over 2H-MoS_2, 1T-2H-MoS_2, 2H-MC, and 1T/2H-MC; and cycling experiments of 1T/2H-MC for PHE, and the results of surface area, pore sizes, pore volumes, comparison of PHE and AQY with previous MoS_2-based photocatalysts, and the results of SSA, k_{app}, and rate constant normalized with SSA (k') (PDF)

AUTHOR INFORMATION

Corresponding Authors

Chuanxiang Chen − *School of Environmental and Chemical Engineering, Jiangsu University of Science and Technology, Zhenjiang 212100, P. R. China*; Email: cxchen@just.edu.cn

Weixin Zou − *State Key Laboratory of Pollution Control and Resource Reuse, School of the Environment, Nanjing University, Nanjing 210023, P. R. China; Jiangsu Key Laboratory of Vehicle Emissions Control, School of Chemistry and Chemical Engineering, Center of Modern Analysis, Nanjing University, Nanjing 210093, P. R. China*; Email: wxzou2016@nju.edu.cn

Xiaoguang Duan − *School of Chemical Engineering and Advanced Materials, The University of Adelaide, Adelaide, South Australia 5005, Australia*; orcid.org/0000-0001-9635-5807; Email: xiaoguang.duan@adelaide.edu.au

Authors

Chengzhang Zhu − *School of Environmental and Chemical Engineering, Jiangsu University of Science and Technology, Zhenjiang 212100, P. R. China*

Qiming Xian − *State Key Laboratory of Pollution Control and Resource Reuse, School of the Environment, Nanjing University, Nanjing 210023, P. R. China*; orcid.org/0000-0002-6965-6425

Qiuying He − *School of Environmental and Chemical Engineering, Jiangsu University of Science and Technology, Zhenjiang 212100, P. R. China*

Cheng Sun − *State Key Laboratory of Pollution Control and Resource Reuse, School of the Environment, Nanjing University, Nanjing 210023, P. R. China*

Shaobin Wang − *School of Chemical Engineering and Advanced Materials, The University of Adelaide, Adelaide, South Australia 5005, Australia*; orcid.org/0000-0002-1751-9162

Complete contact information is available at: https://pubs.acs.org/10.1021/acsami.1c09651

Notes

The authors declare no competing financial interest.

ACKNOWLEDGMENTS

The authors acknowledge the project funded by the National Natural Science Foundation of China (21876078, 21707066), Major Science and Technology Program for Water Pollution Control and Treatment (2017ZX07204004), and the Scientific Research Foundation of Graduate School of Nanjing University (2018CL01). Partial support from Australia Research Council (DE210100253) is also acknowledged.

REFERENCES

(1) Xiao, K. M.; Tsang, T. H.; Sun, D.; Liang, J.; Zhao, H.; Jiang, Z. F.; Wang, B.; Yu, J. C.; Wong, P. K. Interfacing Iodine-Doped Hydrothermally Carbonized Carbon with Escherichia coli through an "Add-on" Mode for Enhanced Light-Driven Hydrogen Production. *Adv. Energy Mater.* **2021**, *11*, 2100291.

(2) Voiry, D.; Salehi, M.; Silva, R.; Fujita, T.; Chen, M. W.; Asefa, T.; Shenoy, V. B.; Eda, G.; Chhowalla, M. Conducting MoS_2 Nanosheets as Catalysts for Hydrogen Evolution Reaction. *Nano Lett.* **2013**, *13*, 6222−6227.

(3) Jiang, Z. F.; Wang, B.; Yu, J. C.; Wang, J. F.; An, T. C.; Zhao, H. J.; Li, H. M.; Yuan, S. Q.; Wong, P. K. $AgInS_2$/$In2S_3$ Heterostructure Sensitization of Escherichia coli for Sustainable Hydrogen Production. *Nano Energy* **2018**, *46*, 234−240.

(4) Che, H. N.; Li, C. M.; Li, C. X.; Liu, C. B.; Dong, H. J.; Song, X. H. Benzoyl Isothiocyanate as a Precursor to Design of Ultrathin and High-Crystalline g-C_3N_4-Based Donor−Acceptor Conjugated Copolymers for Superior Photocatalytic H_2 Production. *Chem. Eng. J.* **2021**, *410*, 127791.

(5) Dong, H. J.; Xiao, M. Y.; Yu, S. Y.; Wu, H. H.; Wang, Y.; Sun, J. X.; Chen, G.; Li, C. M. Insight into the Activity and Stability of RhxP Nano-Species Supported on g-C_3N_4 for Photocatalytic H_2 Production. *ACS Catal.* **2020**, *10*, 458−462.

(6) Tong, H.; Ouyang, S. X.; Bi, Y. P.; Umezawa, N.; Oshikiri, M.; Ye, J. H. Nano-Photocatalytic Materials: Possibilities and Challenges. *Adv. Mater.* **2012**, *24*, 229−251.

(7) Wen, X. J.; Niu, C. G.; Zhang, L.; Liang, C.; Guo, H.; Zeng, G. M. Photocatalytic Degradation of Ciprofloxacin by a Novel Z-Scheme CeO_2−Ag/AgBr Photocatalyst: Influencing Factors, Possible Degradation Pathways, and Mechanism Insight. *J. Catal.* **2018**, *358*, 141−154.

(8) Zhu, C. Z.; Wang, Y. T.; Jiang, Z. F.; Xu, F. C.; Xian, Q. M.; Sun, C.; Tong, Q.; Zou, W. X.; Duan, X. G.; Wang, S. B. CeO_2 Nanocrystal-Modified Layered MoS_2/g-C_3N_4 as 0D/2D Ternary Composite for Visible-Light Photocatalytic Hydrogen Evolution: Interfacial Consecutive Multi-Step Electron Transfer and Enhanced H_2O Reactant Adsorption. *Appl. Catal., B* **2019**, *259*, 118072.

(9) Zhang, Y.-C.; Li, Z.; Zhang, L.; Pan, L.; Zhang, X.; Wang, L.; Aleem, F.-e.; Zou, J.-J. Role of Oxygen Vacancies in Photocatalytic Water Oxidation on Ceria Oxide: Experiment and DFT Studies. *Appl. Catal., B* **2018**, *224*, 101−108.

(10) Ma, Y.; Bian, Y.; Liu, Y.; Zhu, A.; Wu, H.; Cui, H.; Chu, D.; Pan, J. Construction of Z-Scheme System for Enhanced Photocatalytic H_2 Evolution Based on CdS Quantum Dots/CeO_2 Nanorods Heterojunction. *ACS Sustainable Chem. Eng.* **2018**, *6*, 2552−2562.

(11) Chang, K.; Mei, Z. W.; Wang, T.; Kang, Q.; Ouyang, S. X.; Ye, J. H. MoS_2/Graphene Cocatalyst for Efficient Photocatalytic H_2 Evolution under Visible Light Irradiation. *ACS Nano* **2014**, *8*, 7078−7087.

(12) Li, W. Q.; Jin, L.; Gao, F.; Wan, H. Q.; Pu, Y.; Wei, X. Q.; Chen, C.; Zou, W. X.; Zhu, C. Z.; Dong, L. Advantageous Roles of Phosphate Decorated Octahedral CeO_2 {111}/g-C_3N_4 in Boosting Photocatalytic CO_2 Reduction: Charge Transfer Bridge and Lewis Basic Site. *Appl. Catal., B* **2021**, *294*, 120257.

(13) Ding, C. M.; Shi, J. Y.; Wang, Z. L.; Li, C. Photoelectrocatalytic Water Splitting: Significance of Cocatalysts, Electrolyte, and Interfaces. *ACS Catal.* **2017**, *7*, 675−688.

(14) Margarit, C. G.; Asimow, N. G.; Thorarinsdottir, A. E.; Costentin, C.; Nocera, D. G. Impactful Role of Cocatalysts on Molecular Electrocatalytic Hydrogen Production. *ACS Catal.* **2021**, *11*, 4561−4567.

(15) Xia, D. H.; An, T. C.; Li, G. Y.; Wang, W. J.; Zhao, H. J.; Wong, P. K. Synergistic Photocatalytic Inactivation Mechanisms of Bacteria by Graphene Sheets Grafted Plasmonic AgX (X = Cl, Br, I) Composite Photocatalyst under Visible Light Irradiation. *Water Res.* **2016**, *99*, 149−161.

(16) Qiu, B.; Wang, C.; Wang, J.; Lin, Z.; Zhang, N.; Cai, L.; Tao, X.; Chai, Y. Metal-Free Tellurene Cocatalyst with Tunable Bandgap

for Enhanced Photocatalytic Hydrogen Production. *Mater. Today Energy* **2021**, *21*, 100720.
(17) Chen, W. X.; Zhu, X. W.; Zhang, Y. W.; Zhou, Y. M.; Ostrikov, K. Bimetal-Organic Frameworks from In Situ Activated NiFe Foam for highly efficient water splitting. *ACS Sustainable Chem. Eng.* **2021**, *9*, 1826−1836.
(18) Chen, S. Y.; Luo, T.; Chen, K. J.; Lin, Y. Y.; Fu, J. W.; Liu, K.; Cai, C.; Wang, Q. Y.; Li, H.; Li, X. Q.; Hu, J. H.; Li, H. M.; Zhu, M. S.; Liu, M. Chemical Identification of Catalytically Active Sites on Oxygen-doped Carbon Nanosheet to Decipher the High Activity for Electro-synthesis Hydrogen Peroxide. *Angew. Chem., Int. Ed.* **2021**, *60*, 16607−16614.
(19) Zheng, X. L.; Guo, Z. H.; Zhang, G. Y.; Li, H.; Zhang, J. N.; Xu, Q. Building of Lateral/Vertical 1T-2H MoS_2/Au Heterostructure for Enhanced Photoelectrocatalysis and Surface Enhanced Raman Scattering. *J. Mater. Chem. A* **2019**, *7*, 19922−19928.
(20) Apte, A.; Krishnamoorthy, A.; Hachtel, J. A.; Susarla, S.; Idrobo, J. C.; Nakano, A.; Kalia, R. K.; Vashishta, P.; Tiwary, C. S.; Ajayan, P. M. Telluride-Based Atomically Thin Layers of Ternary Two-Dimensional Transition Metal Dichalcogenide Alloys. *Chem. Mater.* **2018**, *30*, 7262−7268.
(21) Zhao, Y. D.; Xu, K.; Pan, F.; Zhou, C. J.; Zhou, F. C.; Chai, Y. Doping, Contact and Interface Engineering of Two-Dimensional Layered Transition Metal Dichalcogenides Transistors. *Adv. Funct. Mater.* **2017**, *27*, 1603484.
(22) Bonaccorso, F.; Colombo, L. G.; Yu, G. H.; Stoller, M.; Tozzini, V.; Ferrari, A. C.; Ruoff, S. R.; Pellegrini, V. Graphene, Related Two Dimensional Crystals, and Hybrid Systems for Energy Conversion and Storage. *Science* **2015**, *347*, 1246501.
(23) Choi, W.; Choudhary, N.; Han, G. H.; Park, J.; Akinwande, D.; Lee, Y. H. Recent Development of Two-Dimensional Transition Metal Dichalcogenides and Their Applications. *Mater. Today* **2017**, *20*, 116−130.
(24) Wu, J. P.; Wang, L.; Zhang, L. Y. Rapid and Nondestructive Layer Number Identification of Two-Dimensional Layered Transition Metal Dichalcogenides. *Rare Met.* **2017**, *36*, 698−703.
(25) Voiry, D.; Fullon, R.; Yang, J.; de Carvalho Castro e Silva, C.; Kappera, R.; Bozkurt, I.; Kaplan, D.; Lagos, M. J.; Batson, P. E.; Gupta, G.; Mohite, A. D.; Dong, L.; Er, D.; Shenoy, V. B.; Asefa, T.; Chhowalla, M. The Role of Electronic Coupling Between Substrate and 2D MoS_2 Nanosheets in Electrocatalytic Production of Hydrogen. *Nat. Mater.* **2016**, *15*, 1003−1009.
(26) Zhang, J. F.; Wang, Y.; Cui, J. W.; Wu, J. J.; Li, Y.; Zhu, T. Y.; Kang, H. R.; Yang, J. P.; Sun, J.; Qin, Y. Q.; Zhang, Y.; Ajayan, P. M.; Wu, Y. C. Water-Soluble Defect-Rich MoS_2 Ultrathin Nanosheets for Enhanced Hydrogen Evolution. *J. Phys. Chem. Lett.* **2019**, *10*, 3282−3289.
(27) He, J.; Chen, L.; Wang, F.; Liu, Y.; Chen, P.; Au, C. T.; Yin, S. F. CdS Nanowires Decorated with Ultrathin MoS_2 Nanosheets as an Efficient Photocatalyst for Hydrogen Evolution. *ChemSusChem* **2016**, *9*, 624−630.
(28) Chia, X. Y.; Eng, A. Y. S.; Ambrosi, A.; Tan, S. M.; Pumera, M. Electrochemistry of Nanostructured Layered Transition-Metal Dichalcogenides. *Chem. Rev.* **2015**, *115*, 11941−11966.
(29) Huang, H.; Cui, Y.; Li, Q.; Dun, C.; Zhou, W.; Huang, W.; Chen, L.; Hewitt, C. A.; Carroll, D. L. Metallic 1T Phase MoS_2 Nanosheets for High-Performance Thermoelectric Energy Harvesting. *Nano Energy* **2016**, *26*, 172−179.
(30) Xu, J.; Zhang, J. J.; Zhang, W. J.; Lee, C. S. Interlayer Nanoarchitectonics of Two-Dimensional Transition-Metal Dichalcogenides Nanosheets for Energy Storage and Conversion Applications. *Adv. Energy Mater.* **2017**, *7*, 1700571.
(31) Merki, D.; Fierro, S.; Vrubel, H.; Hu, X. L. Amorphous Molybdenum Sulfide Films as Catalysts for Electrochemical Hydrogen Production in Water. *Chem. Sci.* **2011**, *2*, 1262−1267.
(32) Li, P.; Zhou, Y.; Li, H. J.; Xu, Q. F.; Meng, X. G.; Wang, X. Y.; Xiao, M.; Zou, Z. G. All-Solid-State Z-Scheme System Arrays of $Fe_2V_4O_{13}$/RGO/CdS for Visible Light-Driving Photocatalytic CO_2 Reduction into Renewable Hydrocarbon Fuel. *Chem. Commun.* **2015**, *51*, 800−803.
(33) Li, J. Z.; Ma, Y.; Ye, Z. F.; Zhou, M. J.; Wang, H. Q.; Ma, C. C.; Wang, D. D.; Huo, P. W.; Yan, Y. S. Fast Electron Transfer and Enhanced Visible Light Photocatalytic Activity Using Multi-Dimensional Components of Carbon Quantum Dots@3D Daisy-Like In_2S_3/Single-Wall Carbon Nanotubes. *Appl. Catal., B* **2017**, *204*, 224−238.
(34) Taniguchi, T.; Sonoda, Y.; Echikawa, M.; Watanabe, Y.; Hatakeyama, K.; Ida, S.; Koinuma, M.; Matsumoto, Y. Intense Photoluminescence from Ceria-Based Nanoscale Lamellar Hybrid. *ACS Appl. Mater. Interfaces* **2012**, *4*, 1010−1015.
(35) Balestrieri, M.; Colis, S.; Gallart, M.; Schmerber, G.; Ziegler, M.; Gilliot, P.; Dinia, A. Photoluminescence Properties of Rare Earth (Nd, Yb, Sm, Pr)-Doped CeO_2 Pellets Prepared by Solid-State Reaction. *J. Mater. Chem. C* **2015**, *3*, 7014−7021.
(36) Acerce, M.; Voiry, D.; Chhowalla, M. Metallic 1T Phase MoS_2 Nanosheets as Supercapacitor Electrode Materials. *Nat. Nanotechnol.* **2015**, *10*, 313−318.
(37) Wang, S.; Zhang, D.; Li, B.; Zhang, C.; Du, Z. G.; Yin, H. M.; Bi, X. F.; Yang, S. B. Ultrastable In-Plane 1T−2H MoS_2 Heterostructures for Enhanced Hydrogen Evolution Reaction. *Adv. Energy Mater.* **2018**, *8*, 1801345.
(38) Lv, R.; Robinson, J. A.; Schaak, R. E.; Sun, D.; Sun, Y. F.; Mallouk, T. E.; Terrones, M. Transition Metal Dichalcogenides and Beyond: Synthesis, Properties, and Applications of Single- and Few-Layer Nanosheets. *Acc. Chem. Res.* **2015**, *48*, 56−64.
(39) Shifa, T. A.; Wang, F.; Liu, Y.; He, J. Heterostructures Based on 2D Materials: A Versatile Platform for Efficient Catalysis. *Adv. Mater.* **2019**, *31*, 1804828.
(40) Zhu, C. Z.; Wei, X. Q.; Li, W. Q.; Pu, Y.; Sun, J. F.; Tang, K. L.; Wan, H. Q.; Ge, C. Y.; Zou, W. X.; Dong, L. Crystal-Plane Effects of CeO_2{110} and CeO_2{100} on Photocatalytic CO_2 Reduction: Synergistic Interactions of Oxygen Defects and Hydroxyl Groups. *ACS Sustainable Chem. Eng.* **2020**, *8*, 14397−14406.
(41) Zou, W. X.; Deng, B.; Hu, X. X.; Zhou, Y. P.; Pu, Y.; Yu, S. H.; Ma, K. L.; Sun, J. F.; Wan, H. Q.; Dong, L. Crystal-Plane-Dependent Metal Oxide-Support Interaction in CeO_2/g-C_3N_4 for Photocatalytic Hydrogen Evolution. *Appl. Catal., B* **2018**, *238*, 111−118.
(42) Li, W. H.; Shen, Y. L.; Xiao, X.; An, C. H.; Wei, G. J.; Wang, Y. Q.; Wang, J. Y.; Wu, Y.; An, C. H. Simple Te-Thermal Converting 2H to 1T@2H MoS_2 Homojunctions with Enhanced Supercapacitor Performance. *ACS Appl. Energy Mater.* **2019**, *2*, 8337−8344.
(43) Yang, F.; Ding, S. P.; Song, H. B.; Yan, N. Single-atom Pd Dispersed on Nanoscale Anatase TiO_2 for the Selective Hydrogenation of Phenylacetylene. *Sci. China Mater.* **2020**, *63*, 982−992.
(44) Xu, C. L.; Yang, Z. F.; Shi, L.; Yin, Y.; Lu, M.; Liu, M. X.; Yuan, A. H.; Wu, H.; Ren, X. M.; Wang, S. B.; Sun, H. Q. Encapsulation of Cuprous/Cobalt Sites in Metal Organic Framework for Enhanced C_2H_4/C_2H_6 Separation. *J. Colloid Interface Sci.* **2021**, *583*, 605−613.
(45) Liu, Y. Y.; Xie, Y.; Liu, L. J.; Jiao, J. L. Sulfur Vacancy Induced High Performance for Photocatalytic H_2 Production over 1T@2H Phase MoS_2 Nanolayers. *Catal. Sci. Technol.* **2017**, *7*, 5635−5643.
(46) Gao, S. Y.; Wang, X. Y.; Song, C. J.; Zhou, S. J.; Yang, F.; Kong, Y. Engineering Carbon-Defects on Ultrathin g-C_3N_4 Allows One-Pot Output via In-Situ Gas-Shocking Approach Dramatically Boosting Photoredox Catalysis Activity. *Appl. Catal., B* **2021**, *295*, 120272.
(47) Mo, Z.; Di, J.; Yan, P. C.; Lv, C. D.; Zhu, X. W.; Liu, D. B.; Song, Y. H.; Liu, C. T.; Yu, Q.; Li, H. M.; Lei, Y. C.; Xu, H.; Yan, Q. Y. An All-Organic D-A System for Visible-Light-Driven Overall Water Splitting. *Small* **2020**, *16*, 2003914.
(48) Zhu, X. W.; Yang, J. M.; Zhu, X. L.; Yuan, J. J.; Zhou, M.; She, X. J.; Yu, Q.; Song, Y. H.; She, Y. B.; Hua, Y. J.; Li, H. M.; Xu, H. Exploring Deep Effects of Atomic Vacancies on Activating CO_2 Photoreduction via Rationally Designing Indium Oxide Photocatalysts. *Chem. Eng. J.* **2021**, *422*, 129888.
(49) Zhu, L. Y.; Li, H.; Xia, P. F.; Liu, Z. R.; Xiong, D. H. Hierarchical ZnO Decorated with CeO_2 Nanoparticles as the Direct Z-Scheme Heterojunction for Enhanced Photocatalytic Activity. *ACS Appl. Mater. Interfaces* **2018**, *10*, 39679−39687.

https://doi.org/10.1021/acsami.1c09651
ACS Appl. Mater. Interfaces 2021, 13, 35818−35827

(50) Hong, Y. Z.; Liu, E. L.; Shi, J. Y.; Lin, X.; Sheng, L. Z.; Zhang, M.; Wang, L. Y.; Chen, J. H. A Direct One-Step Synthesis of Ultrathin g-C_3N_4 Nanosheets from Thiourea for Boosting Solar Photocatalytic H_2 Evolution. *Int. J. Hydrogen Energy* **2019**, *44*, 7194−7204.
(51) Yang, F.; Zhou, L. Z.; Dong, X. X.; Zhang, W. Y.; Gao, S. Y.; Wang, X. Y.; Li, L. L.; Yu, C.; Wang, Q.; Yuan, A. H.; Chen, J. Visible Light-Responsive Nanofibrous α-Fe_2O_3 Integrated FeOx Clusters Templated Siliceous Microsheet for Rapid Catalytic Phenol Removal and Enhanced Antibacterial Activity. *ACS Appl. Mater. Interfaces* **2021**, *13*, 19803−19815.
(52) Lin, B.; Yang, G. D.; Wang, L. Z. Stacking-Layer-Number Dependence of Water Adsorption in 3D Ordered Close-Packed g-C_3N_4 Nanosphere Arrays for Photocatalytic Hydrogen Evolution. *Angew. Chem., Int. Ed.* **2019**, *58*, 4587−4591.
(53) Zou, W. X.; Shao, Y.; Pu, Y.; Luo, Y. D.; Sun, J. F.; Ma, K. L.; Tang, C. J.; Gao, F.; Dong, L. Enhanced Visible Light Photocatalytic Hydrogen Evolution via Cubic CeO_2 Hybridized g-C_3N_4 Composite. *Appl. Catal., B* **2017**, *218*, 51−59.
(54) Cao, Y.; Liu, L. J.; Gao, F.; Dong, L.; Chen, Y. Understanding the Effect of CuO Dispersion State on the Activity of CuO Modified $Ce_{0.7}Zr_{0.3}O_2$ for NO Removal. *Appl. Surf. Sci.* **2017**, *403*, 347−355.
(55) Su, R.; Dimitratos, N.; Liu, J.; Carter, E.; Althahban, S.; Wang, X.; Shen, Y.; Wendt, S.; Wen, X.; Niemantsverdriet, J. W.; Iversen, B. B.; Kiely, C. J.; Hutchings, G. J.; Besenbacher, F. Mechanistic Insight into the Interaction Between a Titanium Dioxide Photocatalyst and Pd Cocatalyst for Improved Photocatalytic Performance. *ACS Catal.* **2016**, *6*, 4239−4247.
(56) Luo, Y. D.; Deng, B.; Pu, Y.; Liu, A. N.; Wang, J. M.; Ma, K. L.; Gao, F.; Gao, B.; Zou, W. X.; Dong, L. Interfacial Coupling Effects in g-C_3N_4/$SrTiO_3$ Nanocomposites with Enhanced H_2 Evolution under Visible Light Irradiation. *Appl. Catal., B* **2019**, *247*, 1−9.
(57) Cai, L.; He, J. F.; Liu, Q. H.; Yao, T.; Chen, L.; Yan, W. S.; Hu, F. C.; Jiang, Y.; Zhao, Y. D.; Hu, T. D.; Sun, Z. H.; Wei, S. Q. Vacancy-Induced Ferromagnetism of MoS_2 Nanosheets. *J. Am. Chem. Soc.* **2015**, *137*, 2622−2627.
(58) Xuyen, N. T.; Ting, J. Hybridized 1T/2H MoS_2 Having Controlled 1T Concentrations and its use in Supercapacitors. *Chem. - Eur. J.* **2017**, *23*, 17348−17355.
(59) Li, M. L.; Zhang, L. X.; Wu, M. Y.; Du, Y. Y.; Fan, X. Q.; Wang, M.; Zhang, L. L.; Kong, Q. L.; Shi, J. L. Mesostructured CeO_2/g-C_3N_4 Nanocomposites: Remarkably Enhanced Photocatalytic Activity for CO_2 Reduction by Mutual Component Activations. *Nano Energy* **2016**, *19*, 145−155.

https://doi.org/10.1021/acsami.1c09651
ACS Appl. Mater. Interfaces 2021, 13, 35818−35827